ELSEVIER

Journal of Fluids and Structures 24 (2008) 1284–1293

JOURNAL OF FLUIDS AND STRUCTURES

www.elsevier.com/locate/jfs

Parametric study of a two degree-of-freedom cylinder subject to vortex-induced vibrations

D. Lucor[a,*], M.S. Triantafyllou[b]

[a]*Institut Jean le Rond d'Alembert, UPMC Univ Paris 06, 4 place Jussieu, 75252 Paris Cedex 05, France*
[b]*Department of Mechanical Engineering, Massachusetts Institute of Technology, 77 Massachusetts Avenue, Cambridge, MA 02139, USA*

Received 31 January 2008; accepted 3 June 2008
Available online 9 September 2008

Abstract

This numerical work is an attempt to build accurate and continuous response surfaces of two degree-of-freedom vortex-induced vibrations (VIV) of flexibly mounted cylinders for a wide range of transverse and in-line natural frequencies. We consider both the structure and the flow to be two-dimensional. The structure has a low mass damping, with the transverse and in-line mass ratios as well as the transverse and in-line damping coefficients being equal. The goal is to capture the sensitivity of the response to the change in the natural frequencies of the structure. The system is studied for a wide range of transverse natural frequency within the synchronization region. The extent of variation of the in-line natural frequency is chosen to be larger than the one of the transverse natural frequency in order to favor multi-modal responses. No preferred frequencies are emphasized within the intervals of study. The numerical technique uses a multi-element stochastic collocation method coupled to a spectral element based deterministic solver.

1. Introduction

Often, only the transverse motion of a cylindrical bluff body subject to VIV is considered in numerical or experimental studies to further simplify the problem. This is supported by the fact that the amplitude of vibrations along the in-line direction is generally much smaller than along the transverse direction when both in-line and transverse natural frequencies of the oscillator are equal. More recently, it was reported that the effect of the in-line motion on the transverse motion can be significant when the natural frequency ratio f_{n_X}/f_{n_Y} departs from one (Sarpkaya, 1995; Dahl et al., 2006). In this case, the presence of the in-line X-motion can cause a severe change in the flow pattern behind the cylinder and might even enhance the transverse Y-motion. The purpose of the present study is to explore the effects of the coupling of the two motions through the interplay of the oscillator natural frequencies. Nevertheless, we will avoid simply collecting an ensemble of numerical simulations for an arbitrary number of possible scenarios, i.e. evaluating the system response for a finite set of structural parameters. Instead, we wish to use a method that will provide us with a continuous representation of the response as a function of the variable parameters. It will hopefully allow us to accurately predict the response for any set of parameters within the domain. Moreover, we wish to generalize the approach and treat the natural frequencies of the oscillator as random quantities; the "random" term, here means, that the frequency values are *uncertain* within certain ranges. This situation may arise due to defective manufacturing

*Corresponding author.
E-mail address: didier.lucor@upmc.fr (D. Lucor).

0889-9746/$ - see front matter © 2008 Elsevier Ltd. All rights reserved.
doi:10.1016/j.jfluidstructs.2008.06.001

processes or complex operational environments. The numerical technique we choose couples a stochastic collocation method, based on the generalized Polynomial Chaos (gPC) representation, to a spectral element based deterministic solver. The power of the gPC representation resides in its ability of assigning a given probability distribution to the parameters (here, the natural frequencies of the oscillator) and to propagate its effects, through the model, to the numerical solution (here, the VIV response). The gPC model then provides fast and efficient approximations of the response and its statistics for any set of natural frequencies within the study interval. The main advantage of the method from a numerical point of view is to reduce the computational cost compared to brute force methods such as Monte-Carlo methods. From a mathematical point of view, the advantage of the method resides in the solid theoretical framework that authorizes an efficient sensitivity analysis of the response.

2. Numerical method

We will first introduce the general framework of the stochastic collocation method. Then we will describe the technique adapted to our fluid-structure interaction problem and briefly present the deterministic solver on which it relies.

2.1. Stochastic collocation method

The gPC representation is a non-statistical method used to solve stochastic differential (SDE) and partial differential equations (SPDE) (Spanos and Ghanem, 1989) and has been used for numerous applications (Ghanem, 1999; Xiu and Karniadakis, 2002; Lucor and Karniadakis, 2004; Lucor et al., 2007). It is a spectral representation of a random process in terms of orthogonal basis functions; the spatial and temporal evolutions of the basis coefficients providing quantitative estimates of the modeled random process solution. It is based on the introduction of the geometry and the coordinates into a probabilistic framework in which the uncertainty of the input parameters and the solution can be quantified. It represents second-order stochastic processes $X(\theta)$ parametrically through a set of independent random variables $\{\chi_j(\theta)\}_{j=1}^{N}, N \in \mathbb{N}$, through the events θ of a random event space Ω. The approach is similar to the variational finite elements formulation for deterministic mechanical problems (Ghanem and Spanos, 1991).

In the following, we will consider a stochastic process $X(\theta)$ that varies over a two-dimensional space (x, y):

$$X(x, y, \theta) = \sum_{k=0}^{\infty} \hat{X}_k(x, y)\Phi_k(\boldsymbol{\chi}(\theta)). \tag{1}$$

Here $\{\Phi_j(\boldsymbol{\chi}(\theta))\}$ are orthogonal polynomials in terms of a *known* zero-mean random vector $\boldsymbol{\chi} := \{\chi_j(\theta)\}_{j=1}^{N}$, satisfying the orthogonality relation $\langle \Phi_i \Phi_j \rangle = \langle \Phi_i^2 \rangle \delta_{ij}$. For our application, we will only keep a finite set of random variables, i.e. $\{\chi_j\}_{j=1}^{N}$ with $N < 3$, and a M finite-term truncation of Eq. (1). Due to its tensor-structure form, a complete basis has $M = (N + P)!/N!P!$ terms, with P being the highest polynomial order in the expansion. We will drop the θ- and spatial dependence of $\boldsymbol{\chi}$ in the following for notation simplicity. We have

$$X(\boldsymbol{\chi}) = \sum_{k=0}^{M-1} \hat{X}_k \Phi_k(\boldsymbol{\chi}), \tag{2}$$

and the $\hat{X}_k$ are the coefficients to determine. The efficiency of the representation depends on the choice of the appropriate parametric family of random variables. Indeed, there exists a close relationship between the type of the orthogonal polynomials $\{\Phi\}$ and the probabilistic law $\rho(\boldsymbol{\chi})$ of the random variables $\boldsymbol{\chi}$. More details on approximating of various class of random variables and correspondence with various class of polynomials and gPC are given in Schoutens (2000) and Xiu and Karniadakis (2002).

Nevertheless, for discontinuous dependence of the solution on the random input data, gPC may converge slowly or fail to converge for long-time integration. This situation arises when the solution is very sensitive to changes in the parameters (e.g. stochastic bifurcation). In this case, the global solution converges slowly even for high order P. One way to circumvent the problem is to decompose the parametric space into N_Ω *non-overlapping* smaller sub-domains Ω_l. Subsequently, in each element we generate a new random variable and apply the gPC technique again. Since the degree of perturbation in each sub-domain is reduced proportionally to its size, we can maintain a relatively low polynomial order and number of terms M_l in each sub-domain. The spectral representation reads:

$$X(\boldsymbol{\chi}) = \sum_{l=1}^{N_\Omega} \sum_{k=0}^{M_l-1} \hat{X}_{l,k}\, \Phi_{l,k}(\boldsymbol{\chi})\, I_{\Omega_l}, \tag{3}$$

where the indicator variable I_{Ω_l} is defined such as: $I_{\Omega_l} = 1$ $(l = 1, 2, \ldots, N_\Omega)$ if $\boldsymbol{\chi} \in \Omega_l$ or $I_{\Omega_l} = 0$ otherwise. We will not describe the multi-elements gPC formulation in more details as it is not the point of the paper. Nevertheless, we can say that its numerical implementation is greatly facilitated in the case of random variables with uniform distributions combined with Legendre polynomials. We refer the interested reader to Wan and Karniadakis (2006b) and we conclude that the method can maintain a desired accuracy by adaptively decomposing the random space as needed.

After solving for the coefficients $\hat{X}_k$, cf. Eq. (2) or $\hat{X}_{l,k}$, cf. Eq. (3), we hold a representation which can be apprehended as a response surface providing with the sensitivity of the solution to the variability of the different parameters. It is then possible to perform a number of analytical operations onto this explicit representation. Moments as well as probability density function (PDF) of the solution can be evaluated. Due to the orthogonality of the modes, the moments can be easily computed. The *mean* solution is contained in the expansion term with zero-index. The second moment, i.e., the *covariance* function is given by a linear combination of the modal fluctuations (Ghanem and Spanos, 1991).

The "non-intrusive" approach or stochastic collocation approach (Tatang et al., 1997) of the gPC application does not require any substantial modifications to the existing deterministic solver. It consists in projecting directly the stochastic solution onto each member of the orthogonal basis chosen to span the random space. The X_k random coefficients take the following form:

$$\forall k \in \{0, \ldots, M-1\}, \quad \hat{X}_k = \frac{\langle X(\boldsymbol{\chi})\Phi_k(\boldsymbol{\chi})\rangle}{\langle \Phi_k^2(\boldsymbol{\chi})\rangle}. \tag{4}$$

The inner product is based on the measure $\rho(\boldsymbol{\chi})$ of the random variables:

$$\langle f(\boldsymbol{\chi})g(\boldsymbol{\chi})\rangle = \int_{\theta\in\Omega} f(\boldsymbol{\chi})g(\boldsymbol{\chi})\,\mathrm{d}\mathscr{P}(\theta) = \int_{\Omega} f(\boldsymbol{\chi})g(\boldsymbol{\chi})\rho(\boldsymbol{\chi})\,\mathrm{d}\boldsymbol{\chi}, \tag{5}$$

with $\rho(\boldsymbol{\chi})$ denoting the density of the law $\mathrm{d}\mathscr{P}(\theta)$ with respect to the Lebesgue measure $\mathrm{d}\boldsymbol{\chi}$ and with integration taken over a suitable domain Ω, determined by the range of $\boldsymbol{\chi}$. We recall that $\langle \Phi_k(\boldsymbol{\chi})\rangle = 0$ for $k > 0$ and the denominator $\langle \Phi_k^2(\boldsymbol{\chi})\rangle$ can be tabulated prior to the projection. The evaluation of Eq. (4) is equivalent to computing multi-dimensional integrals over the domain Ω. Different ways of dealing with high-dimensional integrations can be considered depending on the prevalence of accuracy versus efficiency (Keese, 2005). A convenient approximation consists in numerical quadrature evaluated for some chosen points. When the number of grid points in multi-dimensions N becomes too large, grids based on full tensor products of one-dimensional grids are too costly. An alternative are sparse quadratures (Novak and Ritter, 1999) which require less quadrature points. The sparse quadrature based on Smolyak algorithm (Smolyak, 1963) has the advantage of remaining accurate with a convergence rate depending weakly on N. In this study, we use numerical quadratures of Gauss- and Gauss-Lobatto-type by full tensor products as our number of random dimensions N is small. We insist on the fact that the deterministic solver will compute/provide X at those *known* quadrature points and not at randomly selected locations. The total number of quadrature points N_q to use depends on the regularity of the function to integrate. As there is no way of knowing *a priori* how smooth the solution X will be, we choose to use a minimum number of $N_q = (P+1)^N$ quadrature points for the estimation of all M coefficients.

2.2. Two degree-of-freedom structural model

The nondimensional equations of motion, based on a reference length D (cylinder diameter) and a reference velocity U (inflow velocity), that are solved are:

$$\ddot{X} + 2\zeta_X\omega_X(\theta)\frac{\partial X}{\partial t} + \omega_X^2(\theta)X = \frac{1}{2}\frac{C_{\mathrm{Drag}}(t)}{m_X}, \quad \ddot{Y} + 2\zeta_Y\omega_Y(\theta)\frac{\partial Y}{\partial t} + \omega_Y^2(\theta)Y = \frac{1}{2}\frac{C_{\mathrm{Lift}}(t)}{m_Y}, \tag{6}$$

where $\omega_X(\theta) = 2\pi f_{n_X}(\theta)$ and $\omega_Y(\theta) = 2\pi f_{n_Y}(\theta)$ represent the natural frequencies of the oscillator along the X- and Y-direction respectively. The θ-dependency indicates that the natural frequencies are considered uncertain within the intervals study. The forcing involves the nondimensional time-dependent drag $C_{\mathrm{Drag}}(t)$ and lift $C_{\mathrm{Lift}}(t)$ coefficients, computed iteratively by the flow solver. The hydrodynamic forcing will act as the coupling between these two equations. For all examples considered in this paper, the mass ratios of the structure are: $m_X = m_Y = m = \rho_s/\rho_f D^2 = 2$, ($\rho_s$ is the structural linear density and ρ_f is the fluid volumic density) and the damping ratios are: $\zeta_X = \zeta_Y = \zeta$ with $\zeta = 0$ or $\zeta = 3\%$ depending on the case under consideration. Dimensional frequency values $\hat{f}_n$ may be computed with a proper scaling: $\hat{f}_n = (f_n U)/D$. The reduced velocity of the oscillator is $U_n = U/(\hat{f}_n D)$.

The hydrodynamic loads in Eq. (6) are computed by a 2-D Navier–Stokes direct numerical simulation (DNS) solver, $\mathcal{N}\varepsilon\kappa\mathcal{T}\alpha\tau$, based on a spectral/*hp* element method (Karniadakis and Sherwin, 2005). A Newmark integration scheme is used to solve for the structure. This flow-structure interaction solver was used previously for various challenging VIV

Table 1
Natural frequency and reduced velocity parametric ranges for Case-B

	f_{n_X}	f_{n_Y}	U_{n_Y}	f_{n_X}/f_{n_Y}
Sub-domain 1	[0.127; 0.382]	[0.191; 0.255]	[3.928; 5.236]	[0.5; 2]
Sub-domain 2	[0.127; 0.382]	[0.127; 0.191]	[5.236; 7.856]	[0.667; 3]
Sub-domain 3	[0.382, 0.573]	[0.159, 0.223]	[4.488; 6.281]	[1.714; 3.6]

applications, among others (Lucor and Karniadakis, 2003; Lucor et al., 2005; Dong and Karniadakis, 2005). A two-dimensional rectangular grid of size $[(-22D; 55D) \times (-22D; 22D)]$ in the (x, y)-plane and made of 708 triangular elements (Lucor, 2004) with Jacobi polynomial order $p = 11$ in each grid cell is used. This spatial resolution insures the presence of (at least) 4 computational nodes within the flow boundary layer developing at the wall at $Re = 1000$. Our chosen nondimensional temporal resolution requires at least 10,000 time iterations per period of oscillation. All computations start from the same initial condition where the cylinder is released from rest with zero velocity in a fully developed flow field. Time-statistics are typically collected over approximately 500 to 1500 (when necessary) nondimensional time units, i.e. 100 to 300 oscillation periods. In the following, we focus on the representation of natural frequencies following *uniform* distributions, so that only *bounded* variability ranges are considered and no physical values are "favored" (in a probabilistic sense) within each interval. Legendre polynomials are chosen to represent the response. For stochastic processes that require more than one random dimension, multi-dimensional Legendre polynomials are built in a tensor-like form.

Two generic cases are considered in this study corresponding to different parametric ranges. In the first case (Case-A), we take $f_{n_X} = f_{n_Y} = f_n + \sigma\chi$ where χ follows a uniform distribution with zero mean and unit variance. The parameters f_n and σ are constant parameters referring to the mean value and half the width of the support of the natural frequency, respectively. They are chosen in such a way that f_{n_X} and f_{n_Y} are uniformly distributed in $[0.1114; 0.3024]$. This implies that only one uncertain parameter is considered and $f_{n_X}/f_{n_Y} = 1$ always. The damping factor is $\zeta = 0$. This case will be used in the following as our reference case. In the second case (Case-B), the multi-element approach is used and we distinguish among $N_\Omega = 3$ non-overlapping and non-conforming elements. This domain decomposition has been chosen based on our experience of the system. We will comment and suggest some other possible choices later. In each sub-domain Ω_l, we define the natural frequencies as $f^l_{n_X} = f^l_{n_1} + \sigma^l_1\chi^l_1$ and $f^l_{n_Y} = f^l_{n_2} + \sigma^l_2\chi^l_2$, where χ^l_{1-2} are chosen to be finite independent identically-distributed (iid) uniform random variables with zero mean and unit variance. The parameters $f^l_{n_{1-2}}$ and σ^l_{1-2} are constant and chosen in such way that $f^l_{n_X}$ and $f^l_{n_Y}$ are uniformly distributed according to Table 1. This setup implies that the natural frequencies can both vary independently and that the frequency ratio f_{n_X}/f_{n_Y} in the entire domain is within $[0.5; 3.6]$. A more realistic damping factor of $\zeta = 3\%$ is used for this case.

Those two cases are treated with the combined numerical approach described in Sections 2.1 and 2.2 and some preliminary results are presented in the next section. Any output of the DNS simulations can be treated as a random field and decomposed onto the gPC basis following Eqs. (2) and (3). In the following, we will focus mainly on the cylinder response statistics and its frequency content.

It is worth mentioning that gPC representations of complex and highly nonlinear processes are sometimes inefficient in capturing the right behavior of the system. This is particularly true for long time integration of stochastic systems characterised by a limit cycle oscillation response. For these cases, it was noticed that a spectral decomposition of the solution in terms of global basis exhibits severe limitations (Beran et al., 2006; Wan and Karniadakis, 2006a). In the present study, we propose to circumvent this problem by always considering time-averaged statistical moments of the simulated response and loads as functions of the uncertain parameters, instead of decomposing the time-dependent turbulent pressure and velocity fields themselves.

3. Results

Continuous representations of the cylinder response and loads are constructed with Legendre polynomials. To this end, the collocation procedure described in Section 2.1 needs to evaluate the deterministic solution at some discrete quadrature points in the parametric domain of interest. The DNS solver is therefore run for each *known* sample point, corresponding to a specific pair of natural frequencies, and time-statistics are collected for each case.

3.1. Case-A

Here, a multi-element gPC approach is employed along the lines introduced by Wan and Karniadakis (2006b). Here, we use seven Gauss-Lobatto-quadrature points in each sub-element at which we discretely sample the DNS solution and then up to $P = 5$th order Legendre polynomials to reconstruct the response.

Fig. 1 presents the time traces of the cylinder vertical displacement for different natural frequency pairs. Those signals are quite representative of the possible scenarios encountered in our computations (both Case-A and Case-B). In the first case, the motion eventually settles down to some regular single pattern after some time. This reflects on the cylinder trajectory as well. In the second case, there is a switching among regions characterized by small or large amplitude response that correspond to multiple trajectory patterns. The frequency of occurrence of these regions can be low and/or very irregular. Those cases are the most difficult to simulate and require long time integration. Finally, the last signal is quite irregular at a small time scale but exhibits some stationarity for a long time window. This diversity implies that the temporal statistics collected for each case will not bear the same level of regularity and confidence. In other words, the temporal statistics might not be fully converged for some cases. This will obviously affect the overall accuracy of our study.

Fig. 2 presents the gPC response of the average 10% highest amplitude of the X- and Y-motion against the U_{n_Y} reduced velocity (based on f_{n_Y}). The symbols correspond to the DNS deterministic samplings. The dotted lines delimit the computational sub-domains. The thin dashed curve with circles shows the one degree-of-freedom (1-dof) response of the same system and is used as a reference. We emphasize that a maximum amplitude of $0.6D$ is what is usually reported in the literature and commonly accepted for 2-D direct numerical simulations of 1-dof VIV (Evangelinos, 1999). We notice that allowing in-line motion enhances the maximum transverse cylinder motion relative to transverse-response only, with a 30% increase of the highest amplitude from around $0.6D$ to $0.78D$. Moreover the maximum transverse amplitude of the 2-dof case does not coincide with the one of the 1-dof. We also notice that the gPC interpolation is more continuous and accurate for the Y- than the X-motion, in particular for the $U_{n_Y} \approx [5;7]$ range. Interestingly, the distribution of the in-line amplitude closely follows the same peaks than the transverse amplitude.

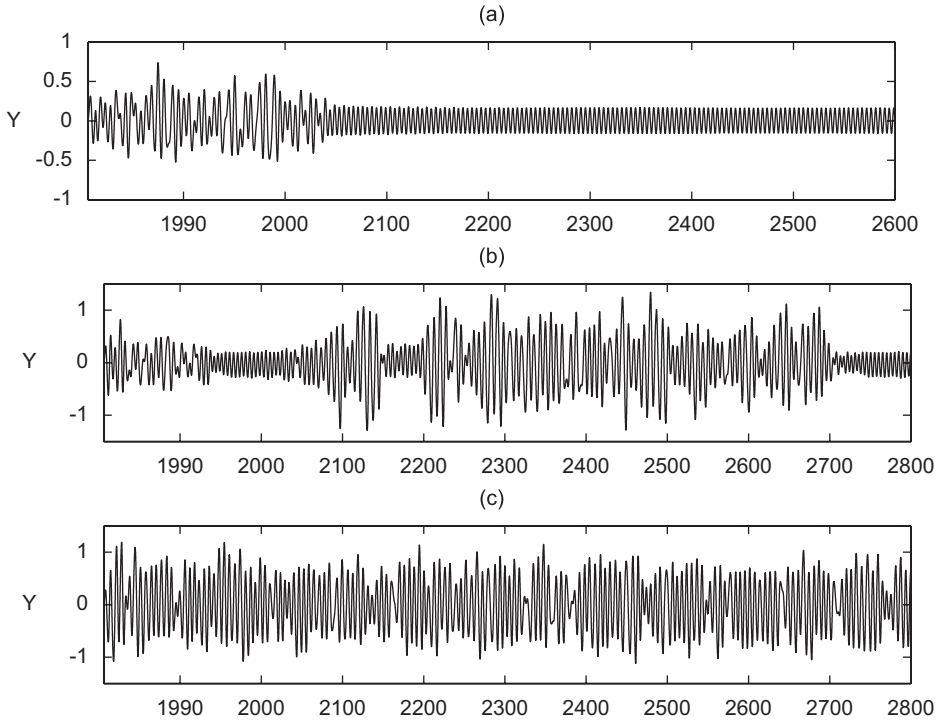

Fig. 1. Time traces of the cylinder transverse Y-motion for different natural frequency pairs (f_{n_X}, f_{n_Y}).

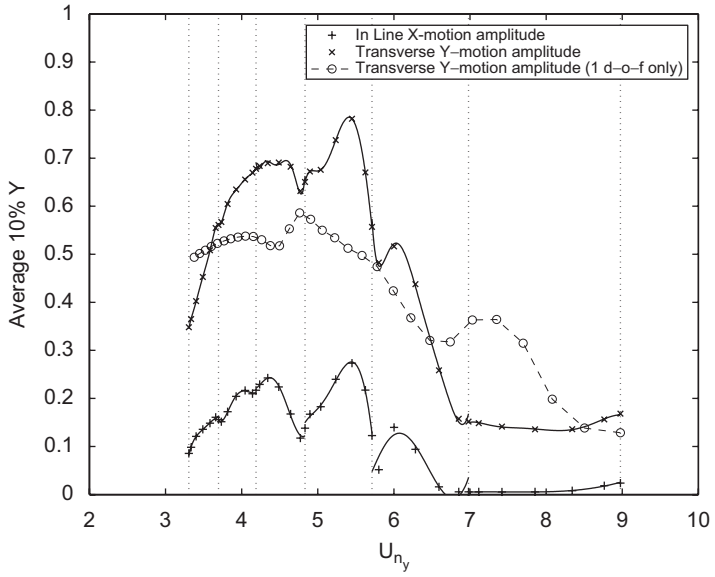

Fig. 2. Average 10% X- and Y-motion highest amplitude responses vs. reduced velocity.

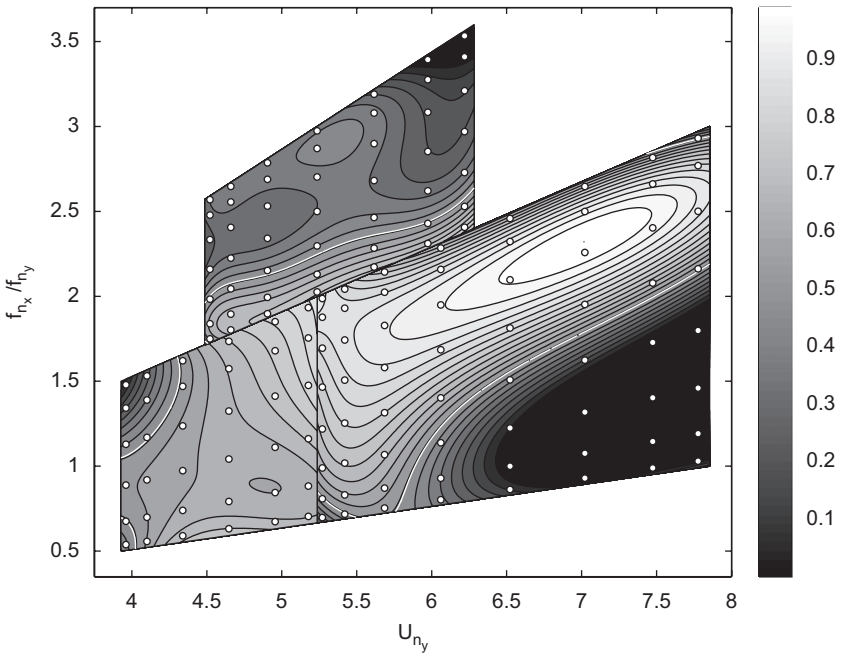

Fig. 3. Response surface of the average 10% Y-motion highest amplitude response vs. reduced velocity and natural frequency ratio. The white dots indicate the location of the sampling/quadrature points. The white line symbolizes the maximum 1-dof response.

3.2. Case-B

Fig. 3 shows the response surface of the average 10% highest amplitude of the Y-motion vs. the reduced velocity U_{n_Y} and the natural frequency ratio f_{n_X}/f_{n_Y}. This way to present the results is in the light of the experimental work of (Dahl et al., 2006). The collocation procedure described in Section 2.1 uses 6 Gauss-quadrature points along each direction for the sub-domain 1 (bottom left). It uses 8^2 for the sub-domain 2 (bottom right) and 7^2 samples for the sub-domain 3 (top). This totals 149 DNS simulations. The deterministic solver is called for each quadrature point on

the map, corresponding to a specific chosen set of parameters (represented by white dots in the figure). The total number of quadrature points per sub-domain was chosen in order to preserve a certain level of resolution depending on the smoothness of the corresponding response surface. However, the multi-element method described in Section 2.1 does not insure exact continuity of this surface across the sub-domains boundaries. This can be seen in Fig. 3 where we use $P = 4$th order Legendre polynomials to reconstruct the response. A measure of the error of the representation is obtained by comparing the exact DNS and gPC reconstructed solutions at the sampling points. In this case, the L_2 norm of the error is within 5% accuracy for sub-domains 1–3 and within 15% accuracy for sub-domain 2. The strong gradients due to parametric bifurcation in the latter explains why the representation somewhat under-predicts the response for large reduced velocities and small frequency ratios. This error can be reduced by increasing P but spurious end-effect oscillations will appear.

The first finding is the increase of the transverse amplitude response compared to the case with no X-motion and Case-A. Indeed, the white line materializes the $0.6D$ amplitude for 1-dof only response. It surrounds a light color region where the crossflow response is large. In this tilted and elongated region, the maximum amplitude is close to one cylinder diameter D for certain combinations of natural frequency and reduced velocity. This corresponds to a 70% increase of the highest amplitude compared to the 1-dof only response and a 25% increase compared to Case-A. In particular, the response is large around $U_{n_Y} \approx 7$ which is consistent with recent 3-D experimental results (Dahl et al., 2006). Nevertheless, this large response for 2-D flow is still below those 3-D results. It is worth mentioning that the maximum amplitude signal within the domain temporarily reached a value of $1.47D$. Moreover, it is clear that increasing the in-line to transverse frequency ratio caused a shift in the peak amplitude response to increasingly higher reduced velocities. This is also in qualitative agreement with Dahl et al. (2006). It was also reported in earlier experiments (Sarpkaya, 1995; Dahl et al., 2006), that two distinct response peaks appear for frequency ratio close to two. At this point, our level of resolution does not allow to check the presence of this double peak. It is also worth mentioning that the damping and mass ratios in Dahl et al. (2006) were slightly different along each direction. Interestingly, for $U_{n_Y} > 5.5$, we notice that the location of the maximum response for a given reduced velocity follows a linear trend. In this case, we have $f_{n_X}/f_{n_Y} \approx 0.4 \times U_{n_Y} - 0.5$. We do not have a conclusive explanation for this phenomenon at the present time but we think it is something worthwhile to pursue.

Another concern relates to the distribution of the possible responses that the system provides within this parametric range. The answer lies in the solution PDF that we construct from the response surface representation. A solution ensemble is generated from Eqs. (2)–(3) and we use a kernel-smoothing density estimate with a Gaussian kernel and an optimal bandwidth (Wand and Jones, 1995) to get the PDFs. Fig. 4 shows the PDFs of the X- and Y-motion amplitude. Here, up to $P = 5$th order Legendre polynomials are used within each sub-domain and a large data set (>5 M) is generated for each PDF. As expected, we observe that the cylinder response is more sensitive along the

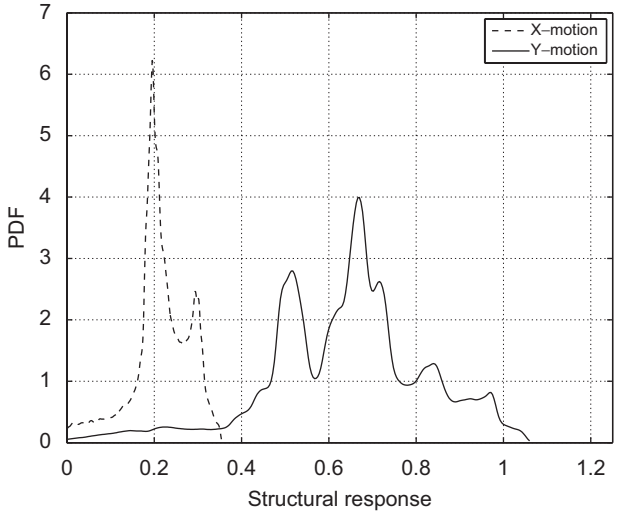

Fig. 4. PDFs of the average 10% X- and Y-motion highest amplitude. The PDF of the X-motion has been rescaled by a factor $1/2$ for figure clarity.

transverse than the in-line direction. Moreover, the PDFs are skewed with longer tails on the side of low amplitudes. The peaks in the distributions indicate the presence of dominant scales within the chosen parametric ranges, leading to the concept of *most probable* solutions. In particular, we notice that amplitude responses in the $0.5D$ and $0.65D$ ranges are most likely to happen for the Y-motion, while $0.2D$ and (to some extent) $0.3D$ amplitudes prevail for the X-motion. From the distribution, we can estimate that there is only a $\approx 23\%$ chance to get a transverse amplitude $>0.75D$, but a $\approx 60\%$ chance to get a transverse amplitude $>0.6D$ (maximum of the 1-dof only response).

Now, we turn our attention to the spectral content of the response. Fig. 5 shows the response surface of the Y-motion dominant oscillation frequency f_Y/f_{n_Y}. In some cases, there were multiple dominant frequencies. We only show the largest magnitude frequency component in this case. This time, the gPC representation is very accurate with a L_2 norm of the error within 5% accuracy for a choice of $P = 5$th. For most of the frequency ratios, the leading frequency increases with increasing nominal reduced velocity in agreement with Dahl et al. (2006). There exists a large portion of the map where $f_Y/f_{n_Y} \approx 1$. On the figure, we have bounded this region (on the right) by a white solid line ($f_Y/f_{n_Y} = 1.2$) and (on the left) by a white dashed line ($f_Y/f_{n_Y} = 0.8$). This gives an idea of the extent of the lock-in region. If we compare this region with Fig. 3, we notice that it partially coincides with the region of large response. More importantly, it shows that the synchronization region becomes wider as nominal frequency ratio is increased. Interestingly, there is no higher harmonics leading the Y-motion oscillation frequency.

This is different when we look at the frequency content of the lift coefficient C_{Lift}. Indeed, if several natural frequencies lie within the excitation band of frequencies, a multi-frequency wide-band response is obtained and high modes are excited. These high modal responses show significant energy at the expected Strouhal frequency as well as at higher harmonics. These phenomena have been observed in measurements from 3-D field experiments, but only recently were they linked to the fatigue of the structure (Vandiver et al., 2006; Dahl et al., 2007). Fig. 6 illustrate the response surfaces of the C_{Lift} high-frequency component contributions. Here, the power spectrum density has been integrated over a finite range and normalized by the total power spectrum of the signal. A value close to unity indicates that most of the energy content resides within this frequency range. Each graph corresponds to a different range defined to tightly bound the harmonics of the crossflow natural frequency of the structure. This time, we notice that the higher harmonics contribution to the C_{Lift} coefficient is far from being negligible for some parametric ranges. In particular the 3rd harmonic is dominant for relatively low reduced velocity and large frequency ratio (cf. Fig. 6(c)). This is again consistent with the results of Dahl et al. (2006) and Jauvtis and Williamson (2004). We also observe the presence of a strong ($>40\%$) 4th harmonic for higher reduced velocity and frequency ratio close to 3 (cf. Fig. 6(d)).

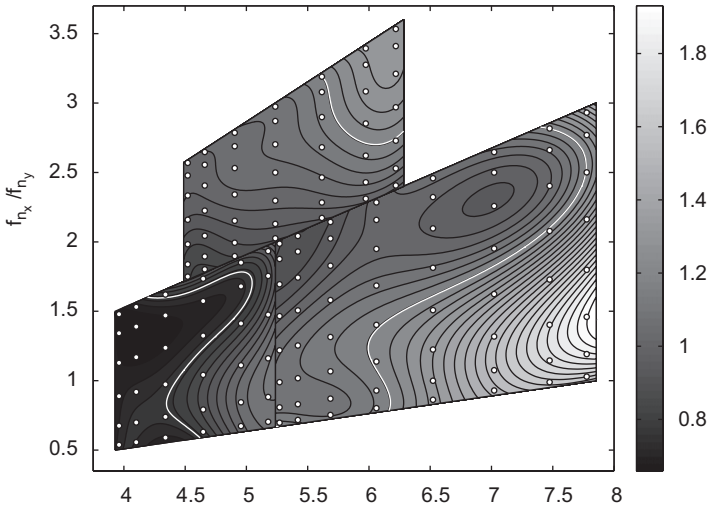

Fig. 5. Response surface of the Y-motion leading oscillation frequency f_Y/f_{n_Y} vs. reduced velocity and natural frequency ratio. The white dots indicate the location of the sampling/quadrature points. The solid white line delineates a frequency ratio of $f_Y/f_{n_Y} = 1.2$ while the dashed white line delineates a frequency ratio of $f_Y/f_{n_Y} = 0.8$.

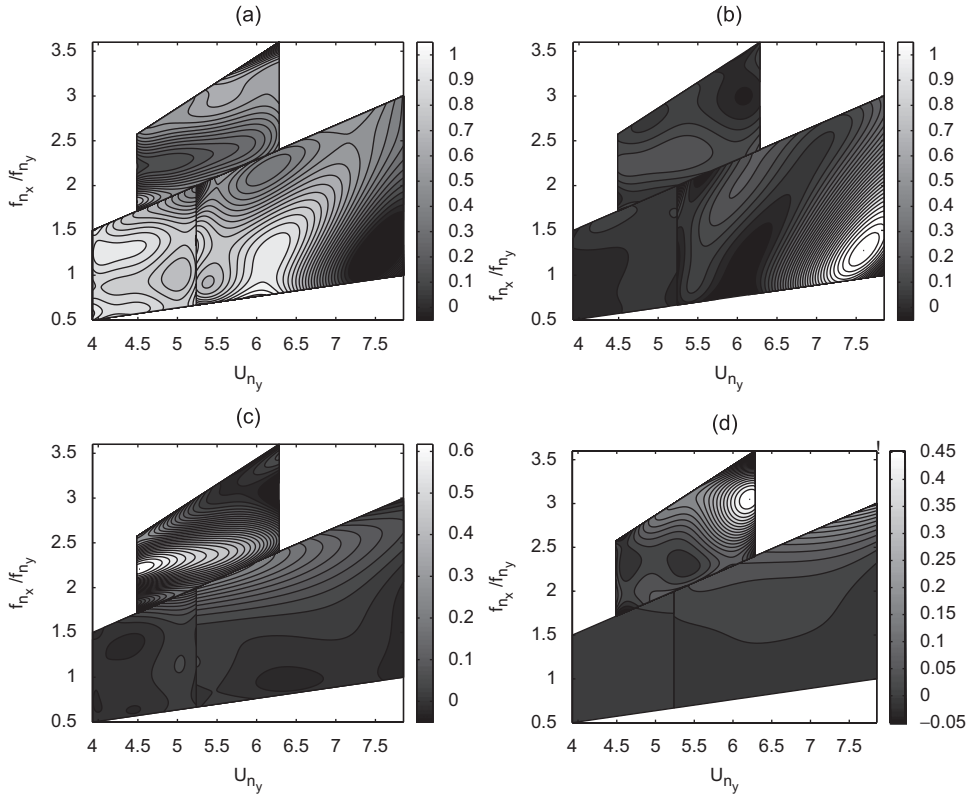

Fig. 6. Response surfaces of the C_{Lift} high-frequency components relative contribution. (a) 1st harmonic; (b) 2nd harmonic; (c) 3rd harmonic and (d) 4th harmonic.

4. Conclusions

This is a first attempt to apply recent numerical stochastic collocation techniques to 2-dof VIV of flexibly mounted cylinders. The goal is to capture the response sensitivity to the change in both transverse and in-line natural frequencies of the oscillator. The system is sampled for a wide range of natural frequency within the synchronization region, totalizing 149 2-D flow-structure DNS. No preferred frequencies are emphasized within the intervals of study. We then derive a continuous response surface of the system response. Here are our main conclusions in agreement with 3-D experimental results (Dahl et al., 2006). We have noticed an increase of the transverse response compared to the case with no in-line motion and the 2-dof case with equal natural frequencies. There exists a large parametric region in which the average 10% highest transverse amplitude is close to $1D$ for certain combinations of natural frequency and reduced velocity. While this corresponds to a 70% increase compared to the 1-dof only, it is still below 3-D experimental results with maximum amplitude as high as $1.35D$ and above. The response is particularly large for $U_{n_Y} \approx 7$. The spectral analysis of the response dominant frequency permitted to identify the extent of the lock-in region that coincides with the region of large response. We have found that the maximum response was obtained due to lift forces locked to the transverse motion but with significant 3rd harmonic frequency component. Indeed, response surfaces of the lift high-frequency component have shown nontrivial contributions from the 3rd and 4th harmonics for some parametric ranges. Besides, it is clear that increasing the in-line to transverse frequency ratio widened the synchronization region and caused a shift in the peak amplitude response to increasingly higher reduced velocities.

Moreover, for sufficiently large transverse reduced velocity, we have noticed that the frequency ratio for which the response is maximum follows a linear trend. Finally, we have also produced distributions of the transverse and in-line motion amplitudes. The distributions indicate the presence of dominant scales within the chosen parametric ranges, leading to the concept of *most probable* solutions.

Differences with 3-D experimental results are as follows: our maximum response region was obtained for a frequency ratio close to 2.25; this value is lower for the experiments. Moreover, it was reported in earlier experiments, that two distinct response peaks appear for frequency ratio close to 2. Our level of resolution does not allow to verify the presence of this double peak.

It is known that 2-D simulations of 1-dof VIV show inherent limitations when compared to 3-D results. Hopefully, this study will help quantifying the level of trust that one can give to 2-D numerical simulations of 2-dof VIV. Finally, those results will guide us to pursue a, computationally more costly, three-dimensional study of the same phenomenon. In our future work, the impact of the change in the in-line natural frequency on the phase between the transverse response and the in-line response will be discussed and linked to flow visualizations.

Acknowledgement

The authors acknowledge with gratitude support by the BP-MIT Major Projects Program, and by ONR Grant N00014-04-0009, monitored by Thomas Swean, Jr.

References

Beran, P., Pettit, C., Millman, D., 2006. Uncertainty quantification of limit-cycle oscillations. Journal of Computational Physics 217 (1), 217–247.

Dahl, J., Hover, F., Triantafyllou, M., 2006. Two-degree-of-freedom vortex-induced vibrations using a force assisted apparatus. Journal of Fluids and Structures 22, 807–818.

Dahl, J., Hover, F., Triantafyllou, M., Dong, S., Karniadakis, G., 2007. Resonant vibrations of bluff bodies cause multi-vortex shedding and high frequency forces. Physical Review Letters 99 (14), 144503.

Dong, S., Karniadakis, G., 2005. DNS of flow past a stationary and oscillating cylinder at $Re = 10000$. Journal of Fluids and Structures 20, 519–531.

Evangelinos, C., 1999. Parallel simulations of vortex-induced vibrations in turbulent flow: linear and non-linear models. Ph.D. Thesis, Division of Applied Mathematics, Brown University.

Ghanem, R., 1999. Ingredients for a general purpose stochastic finite element formulation. Computer Methods in Applied Mechanics and Engineering 168, 19–34.

Ghanem, R., Spanos, P., 1991. Stochastic Finite Elements: A Spectral Approach. Springer-Verlag.

Jauvtis, N., Williamson, C., 2004. The effect of two degrees of freedom on vortex-induced vibration at low mass and damping. Journal of Fluid Mechanics 509, 23–62.

Karniadakis, G., Sherwin, S., 2005. Spectral/hp Element Methods for CFD, 2nd ed. Oxford University Press, Oxford.

Keese, A., 2005. Numerical solution of systems with stochastic uncertainties: a general purpose framework for stochastic finite elements. Ph.D. Thesis, Technische Universität Braunschweig, Mechanik-Zentrum.

Lucor, D., 2004. Generalized polynomial chaos: applications to random oscillators and flow-structure interactions. Ph.D. Thesis, Brown University, RI, USA.

Lucor, D., Karniadakis, G., 2003. Effects of oblique inflow in vortex induced vibrations. Flow, Turbulence and Combustion 71, 375–389.

Lucor, D., Karniadakis, G., 2004. Noisy inflows cause a shedding-mode switching in flow past an oscillating cylinder. Physics Review Letters 92 (15), 154501-1; 154501-4.

Lucor, D., Foo, J., Karniadakis, G., 2005. Vortex mode selection of a rigid cylinder subject to VIV at low mass-damping. Journal of Fluids and Structures 20, 483–503.

Lucor, D., Meyers, J., Sagaut, P., 2007. Sensitivity analysis of LES to subgrid-scale-model parametric uncertainty using polynomial chaos. Journal of Fluid Mechanics 585, 255–279.

Novak, E., Ritter, K., 1999. Simple cubature formulas with high polynomial exactness. Constructive Approximation 15, 499–522.

Sarpkaya, T., 1995. Hydrodynamic damping, flow-induced oscillations, and biharmonic response. ASME Journal of Offshore Mechanics and Arctic Engineering 117, 232–238.

Schoutens, W., 2000. Stochastic Processes and Orthogonal Polynomials. Springer-Verlag, New York.

Smolyak, S., 1963. Quadrature and interpolation formulas for tensor products of certain classes of functions. Soviet Mathematics, Doklady 4, 240–243.

Spanos, P., Ghanem, R., 1989. Stochastic finite element expansion for random media. ASCE Journal of Engineering Mechanics 115 (5), 1035–1053.

Tatang, M., Pan, W., Prinn, R., McRae, G., 1997. An efficient method for parametric uncertainty analysis of numerical geophysical models. Journal of Geophysical Research 102, 21925–21932.

Vandiver, J., Swithenbank, S., Jaiswal, V., Jhingran, V., 2006. Fatigue damage from high mode number vortex-induced vibration. In: Proceedings of the 25th International Conference on Offshore Mechanics and Arctic Engineering. Hambourg, Germany.

Wan, X., Karniadakis, G., 2006a. Long-term behavior of polynomial chaos in stochastic flow simulations. Computer Methods in Applied Mechanics and Engineering 195, 5582–5596.

Wan, X., Karniadakis, G., 2006b. Multi-element generalized polynomial chaos for arbitrary probability measures. SIAM Journal on Scientific Computing 28 (3), 901–928.

Wand, M., Jones, M., 1995. Kernel smoothing. Monographs on Statistics and Applied Probability 60. Chapman and Hall/CRC.

Xiu, D., Karniadakis, G., 2002. The Wiener-Askey polynomial chaos for stochastic differential equations. SIAM Journal on Scientific Computing 24 (2), 619–644.